Cell Reports
Physical Science

CellPress
OPEN ACCESS

Article

Conductive hollow hydrogel fibers toward high-sensitivity bio-textiles

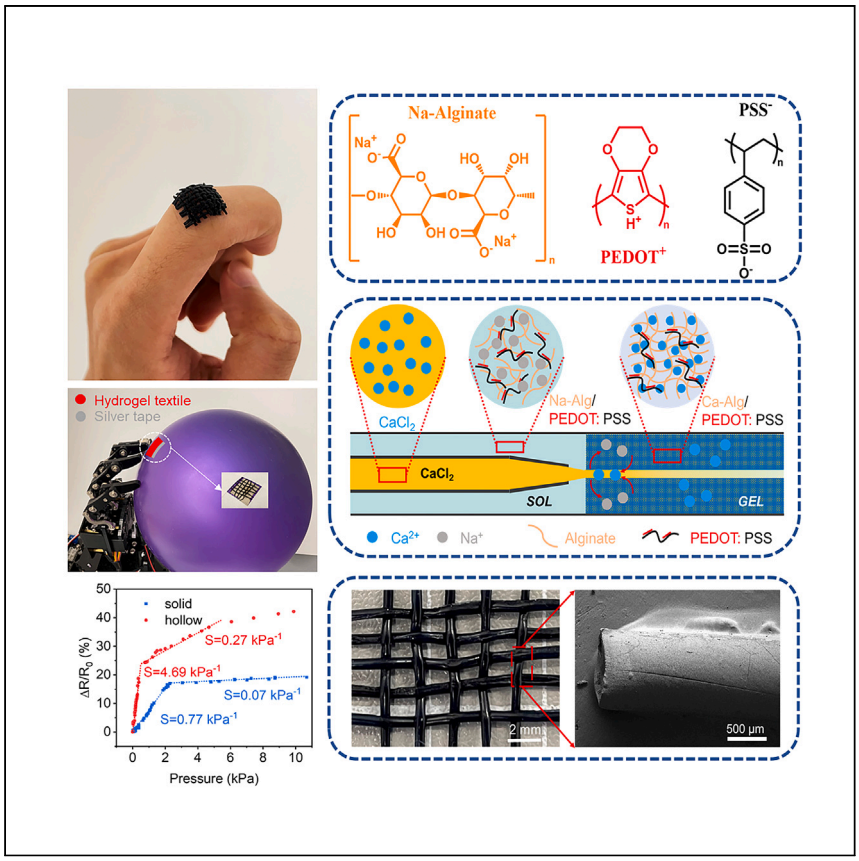

Deng et al. develop a conductive breathable bio-textile with hollow hydrogel fibers using co-axial microfluidics. This hollow structured textile offers 6 times the sensitivity of the solid counterparts and can be used for motion detection and energy harvesting. This advancement promises improved comfort and functionality in wearable sensors and bio-interface applications.

Pengfei Deng, Zijian He, Yingnan Shen, Noor Mohammad Mohammad, Wenhui Xu, Bumsoo Han, Tian Li

tianli@purdue.edu

Highlights

Hollow hydrogel fibers are controllably printed using co-axial microfluidics

Hollow structured fibers show 6× sensitivity compared to solid fibers

Bio-textile achieves high sensitivity and breathability for motion detection

Hydrogel fibers can be applied in energy harvesting

Deng et al., Cell Reports Physical Science 5, 102047
July 17, 2024
https://doi.org/10.1016/j.xcrp.2024.102047

Cell Reports
Physical Science

CellPress
OPEN ACCESS

Article

Conductive hollow hydrogel fibers toward high-sensitivity bio-textiles

Pengfei Deng,[1] Zijian He,[1] Yingnan Shen,[1] Noor Mohammad Mohammad,[1] Wenhui Xu,[1] Bumsoo Han,[1,2] and Tian Li[1,3,*]

SUMMARY

Conductive hydrogels are becoming valuable in creating soft, flexible interfaces for biological tissue sensing due to their bio-compatibility and tissue-like mechanical properties. However, when tailored to epidermal sensors, they face low breathability and sensitivity issues, impacting long-term comfort and functionality. Addressing these issues, here we report sensing textiles from hollow conductive hydrogel fibers using co-axial microfluidic printing, allowing precise control of hollow channel diameters. The mesh-like textile demonstrates a sensitivity of 4.69 kPa^{-1}, significantly outperforming the solid-structured counterparts (0.77 kPa^{-1}). Moreover, the bio-textile demonstrates bio-compatibility, exhibiting no significant cytotoxic effects on human dermal fibroblasts after 3 days. To enhance durability and reusability, we integrate conductive fibers with metal wires for energy harvesting, achieving an open-circuit voltage output of ~0.74 V. Notably, the voltage remains at ~0.53 V even after dehydration. The high sensitivity, softness, and flexibility make our bio-textile a promising candidate for multifunctional sensing and energy harvesting in bio-interface devices.

INTRODUCTION

With the advent of artificial intelligence and the Internet of Things, recent research has made significant progress in developing flexible sensors capable of real-time monitoring of mechanical stimuli like pressure[1–3] and strain,[4,5] as well as physiological stimuli.[6–8] These sensors, owing to their unique properties, such as bendability, stretchability, high sensitivity,[9,10] waterproofness,[11,12] and ability to maintain functionality under various conditions,[13–15] play a crucial role in diverse applications. Among them, hydrogel-based bio-interface devices capable of bio-mechanical detection have attracted increasing scientific attention due to their inherent biocompatibility and adjustable mechanical properties, including a low Young's modulus (1–10^2 kPa), enabling their integration with biological tissues.[16–18] Recent advancements have explored the combination of these hydrogels with electrically conductive polymers or inorganic materials to form conductive hydrogels. These innovative materials find applications across various domains, including bio-electronics,[19–21] soft sensors,[22,23] actuators,[24,25] energy storage devices,[26,27] etc.

Sensitivity and breathability are recognized as the critical properties of bio-interface conductive hydrogels, especially for their use in wearable or implantable devices. Sensitivity ensures functional efficiency in detecting and responding to external stimuli, while breathability ensures the compatibility, comfort, and health of the tissues interfacing with the hydrogel. However, ensuring both sensitivity and breathability, crucial for wearable or implantable devices, remains a challenge due

[1]School of Mechanical Engineering, Purdue University, West Lafayette, IN 47907, USA

[2]Department of Mechanical Science and Engineering and Materials Research Laboratory, University of Illinois Urbana-Champaign, Urbana, IL 61801, USA

[3]Lead contact

*Correspondence: tianli@purdue.edu

https://doi.org/10.1016/j.xcrp.2024.102047

to the inherent structure of solid hydrogels being filled with water, resulting in reduced air permeability and the formation of impermeable 2D films or bulk structures.[28–30]

To address the breathability issue, fiber-like materials, driven by their potential to be woven into mesh-like textiles, have emerged as promising solutions.[31–33] The textiles, leveraging the inherent breathability of their air-circulating design and tissue-like mechanical properties, offer an innovative solution for bio-interface devices where breathability and softness are desired.[34–36] Yet, achieving high-performance hydrogel textiles at scale necessitates continuous high-throughput manufacturing of functional hydrogel fibers. Li et al.[37] reported a robust and flexible ionic aromatic polyimide (PI) hydrogel applied as a strain sensor in response to high-speed motion fiber using a facile wet spinning method. Similarly, Shuai et al.[38] developed an energy-harvesting poly(N-acryloylglycinamide-co-acrylamide) (PNA) hydrogel textile through a dry-wet spinning strategy, capable of strain sensing via thermally reversible sol-gel transition. Despite this progress, the reported hydrogel fibers often exhibit reduced sensitivity due to their solid composition and the absence of intricate internal microstructures. Therefore, research in achieving breathable and sensitive hydrogels via a facile high-throughput method remains important.

Our study addresses these limitations by modulating the microstructural nuances within hydrogel fibers, potentially augmenting their deformation response and sensitivity while providing a unique blend of softness, bio-compatibility, and breathability. This work explores co-axial microfluidic printing to fabricate conductive hollow hydrogel fibers, providing an effective way of devising functional fibers with high printing resolution, shape fidelity, and flexibility due to their versatile and easily controllable properties.[39–41] This process involves the simultaneous flow of two immiscible fluids, a hydrogel precursor solution of sodium alginate (Na-Alg) and a non-reactive solvent of calcium chloride ($CaCl_2$), through a microfluidic channel (Figure 1A). To enhance the conductivity of the fabricated fibers, poly(3,4-ethylenedioxythiophene):polystyrene sulfonate (PEDOT:PSS) is mixed with Na-Alg and evenly distributed within the hydrogel network. Within the channel, sodium ions are substituted with calcium ions, causing alginate molecules to bind and form calcium alginate (Ca-Alg) (Figure 1B). The dimensions and geometry of the enclosed microfluidic channels within the hollow hydrogel fibers are precisely controlled by the fine modulation of flow rates of the involved fluids. Finally, these fibers are woven into a mesh-like 2D structure to create a soft, adhesive, permeable, and breathable sensing textile (Figure 1C). Compared to solid hydrogel films, our woven-structured textile hydrogel demonstrates improved permeability and breathability, as illustrated in Figure S1.

The resulting hollow hydrogel textile exhibits a sensitivity of 4.69 kPa^{-1}, a significant improvement of a 5-fold increase compared to the solid structure (0.77 kPa^{-1}), attributable to the unique mechanical properties of the hollow hydrogel fibers, i.e., their excellent deformation response, enabling effective detection of motion and deformation. Our findings suggest that incorporating a hollow structure can significantly enhance sensitivity, offering the potential for improving the performance of previously reported woven hydrogel works (Table S1), despite their already achieved high sensitivity. Furthermore, this study demonstrates a potential avenue to leverage the inherent long-term dehydration, often considered a drawback of conductive hydrogels, for energy harvesting applications. By combining the conductive fibers with metal wires, the system achieved an open-circuit voltage output of ~0.53 V even when the hydrogel is dehydrated. Moreover, since the

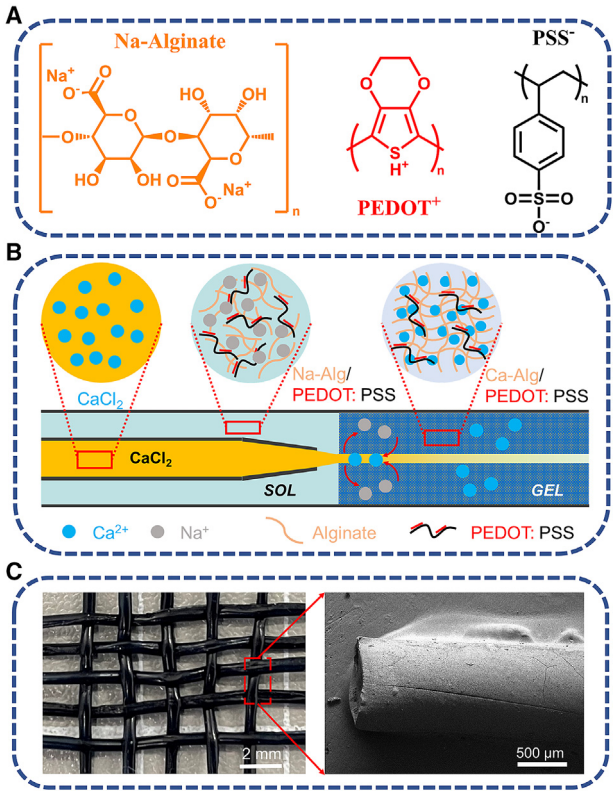

Figure 1. Illustration of the conductive hollow hydrogel textile and its fabrication

(A) Chemical structure of Na-Alg and PEDOT:PSS.

(B) Schematic of the co-axial microfluidic printing method to fabricate conductive hollow hydrogel fibers with hollow structure.

(C) Photograph of 2D mesh-like hydrogel textile (left) (scale bar: 2 mm) and SEM image of conductive hollow hydrogel fiber (right) (scale bar: 500 μm).

manufacturing is based on continuous, cost-effective, and easily scalable additive manufacturing with precise control over fiber geometry and hollow structure dimensions, this study holds potential for next-generation wearable devices, bio-interface sensors, soft devices for human-robot interactions, and electronic skin for prosthetic limbs.

RESULTS

Co-axial microfluid printing for hollow hydrogel fibers

Co-axial microfluidic printing has emerged as a transformative manufacturing methodology, especially for bio-electronic applications, offering a multitude of advantages such as controlled multilayer deposition, diverse material selection, and fast prototyping. Our research harnesses this methodology by integrating a two-phase flow, core-phase fluid and sheath-phase fluid, via a spinneret (Figure 2A). The spinneret manufactured by stereolithography (SLA) 3D printing for easy diameter adjustments (Figure S2) facilitates the introduction of a hydrogel precursor, 2 wt % Na-Alg solution mixed with 0.65 wt % PEDOT:PSS, into the sheath channel via the upper inclined entrance. Concurrently, the core-phase flow, containing 2 wt % $CaCl_2$ as a cross-linker, was transported through capillary tubes into the core channel. At the merging point, a stable laminar flow fostered *in situ* gelation of Ca-Alg with the diffused Ca^{2+} ions from the non-viscous core-phase fluid through diffusion, a process facilitated by hydrodynamic focusing. This process allows the core-phase fluid

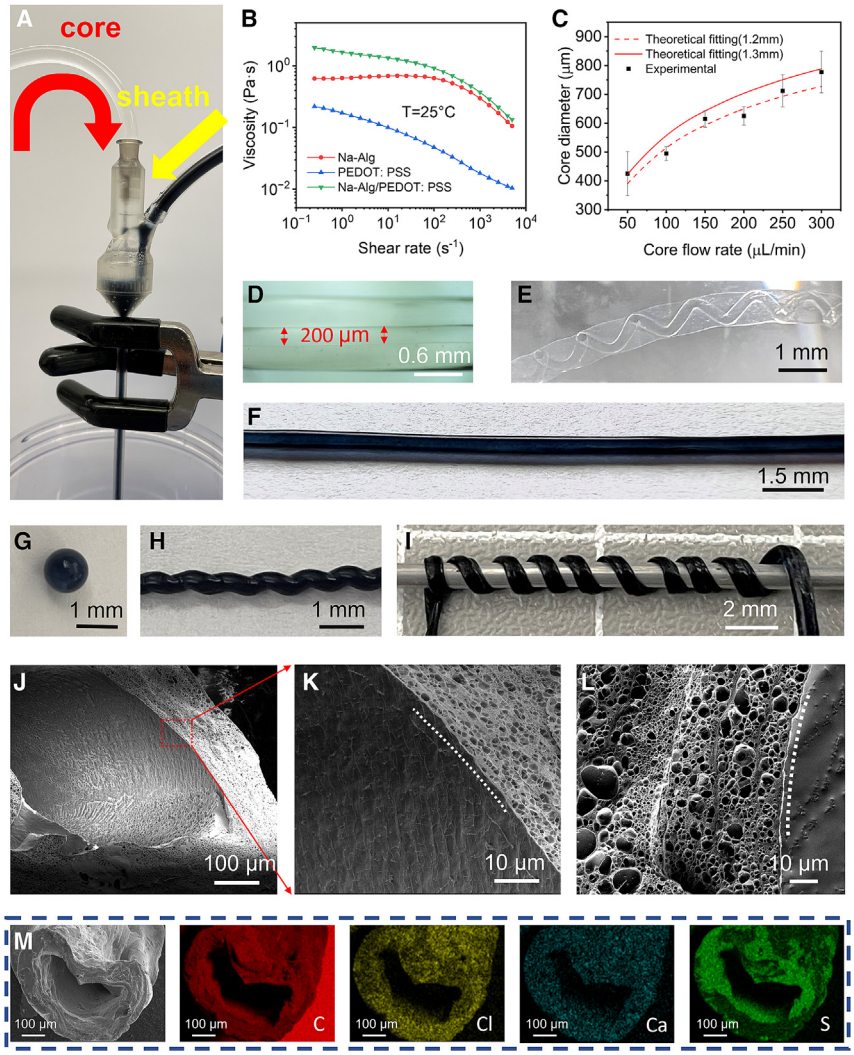

Figure 2. Co-axial microfluid printing process and conductive hollow hydrogel fiber

(A) Picture depicting the co-axial microfluidic printing tube.

(B) Rheological behavior of Na-Alg, PEDOT:PSS, and their mixture.

(C) Experimental and theoretical fitting of the relationship between core diameter and core-phase flow rate in pure alginate hydrogel fibers (data are represented as means ± SD).

(D and E) Optical images of the Ca-Alg hollow hydrogel fiber with straight (D) (scale bar: 0.6 mm) and helical (E) (scale bar: 1 mm) inner structures.

(F–I) Optical images of the Ca-Alg/PEDOT:PSS conductive hydrogel in different shapes: 1D fiber (F) (scale bar: 1.5 mm), 0D dot (G) (scale bar: 1 mm), spiral (H) (scale bar: 1 mm), and wrapped (I) (scale bar: 2 mm).

(J) Cryo-SEM images showing the hollow channel of the printed conductive hollow hydrogel fibers (scale bar: 100 μm).

(K–L) Cryo-SEM images showing the porous channel walls of the printed conductive hollow hydrogel fibers (scale bar: 10 μm).

(M) EDX images of Ca-Alg/PEDOT:PSS conductive hollow hydrogel fiber (scale bar: 100 μm).

to coalesce co-axially within the sheath fluid, leading to the continuous spinning of alginate microfibers.[42,43]

The laminar flow at the entrance was confirmed by the low Reynolds numbers and the demonstrated rheological behavior of 4 wt % Na-Alg, 1.3 wt % PEDOT:PSS,

and their 1:1 weight ratio mixture (Figure 2B). These fluids exhibited shear-thinning behavior, a decrease of viscosity η with respect to shear, a phenomenon attributable to the entangled chain networks in the polymer solution.[44] Moreover, the mixture fluid, the basis of the hydrogel textile, displayed a higher viscosity, indicating a lower Reynolds number ranging between ~0.00068 and 0.059, establishing the presence of laminar flow in the system.[45]

The critical aspect of this process lies in controlling the core diameter of the conductive hydrogels. This process defines the resulting fiber's strength, conductivity, and stretchability and tailors them to meet application-specific requirements. This study deduces the relationship between the channel diameters and the corresponding flow rates. The spinneret's sheath-phase flow rate and inner diameter are 200 μL/min and 1.5 mm, respectively. The instantaneous reaction enables the formation of the hydrogel sheath, where the inner non-viscous channel is maintained due to the tension between the solid-liquid interfaces. The experimental correlation between the core diameter and the core flow rate revealed that the printed solid hydrogel fibers exhibited a 0.1 mm shrinkage (Figure S3), which could be attributable to extrusion contractions. Moreover, a theoretical curve has been fitted to understand the core adjustment behavior further, using Equation 1 derived from the Navier-Stokes equation (Note S2):

$$\frac{D_{core}}{D} = \left[1 - \left(\frac{Q_{sheath}}{Q_{core}+Q_{sheath}}\right)^{\frac{1}{2}}\right]^{\frac{1}{2}} \quad \text{, (Equation 1)}$$

where Q_{core} is the core-phase flow rate and Q_{sheath} is the sheath-phase flow rate.

The geometry of the hollow structure can also be regulated. Studies indicated that when the Q_{sheath} is more than the Q_{core}, the hollow structure will be helical, which comes from the hetero-generated rope-coil effect. Conversely, a lower ratio of Q_{sheath}/Q_{core} leads to a straight hollow structure.[40] As is shown in Figure 2C, the experimental results (Figures S4–S10) of the adjustable core diameter as a function of Q_{core} fit well with the theoretical results. Therefore, fibers produced with varying core flow rates (e.g., 100, 200, and 300 μL/min) have been categorized based on their theoretical inner diameters (e.g., 514, 650, and 728 μm) throughout this paper. Furthermore, by adjusting the Q_{sheath} used in previous experiments and regulating the ratio of Q_{sheath}/Q_{core}, both straight hollow structures with a core diameter as low as 200 μm (Figure 2D) and helical core structures (Figure 2E) in pure Ca-Alg were successfully printed. Subsequently, PEDOT:PSS with Na-Alg was integrated into the hollow structures to form the conductive hollow hydrogel fibers (Figure 2F). Additionally, as shown in Figures 2G–2I, benefiting from the simple adjustable process and the tunability of the hydrogel fibers, the conductive hydrogel was prepared for different shapes, demonstrating its vast potential across diverse application scenarios.

To delve deeper into the internal morphological structure of the hollow and shell components, we conducted scanning electron microscopy in cryogenic mode (cryo-SEM). Figures 2J and S11 show SEM images of the hollow structure with different diameters within the conductive hydrogel fibers, fabricated using different core flow rates. Furthermore, SEM analysis (Figures 2K and 2L) revealed a smooth cylindrical channel (the boundary is indicated in a white dash), showcasing smaller and more densely distributed pores near the inner side compared to the outer side. Energy dispersive X-ray analysis (EDX) elemental mapping confirmed the elemental composition, with Ca and S mapping indicating the existence and

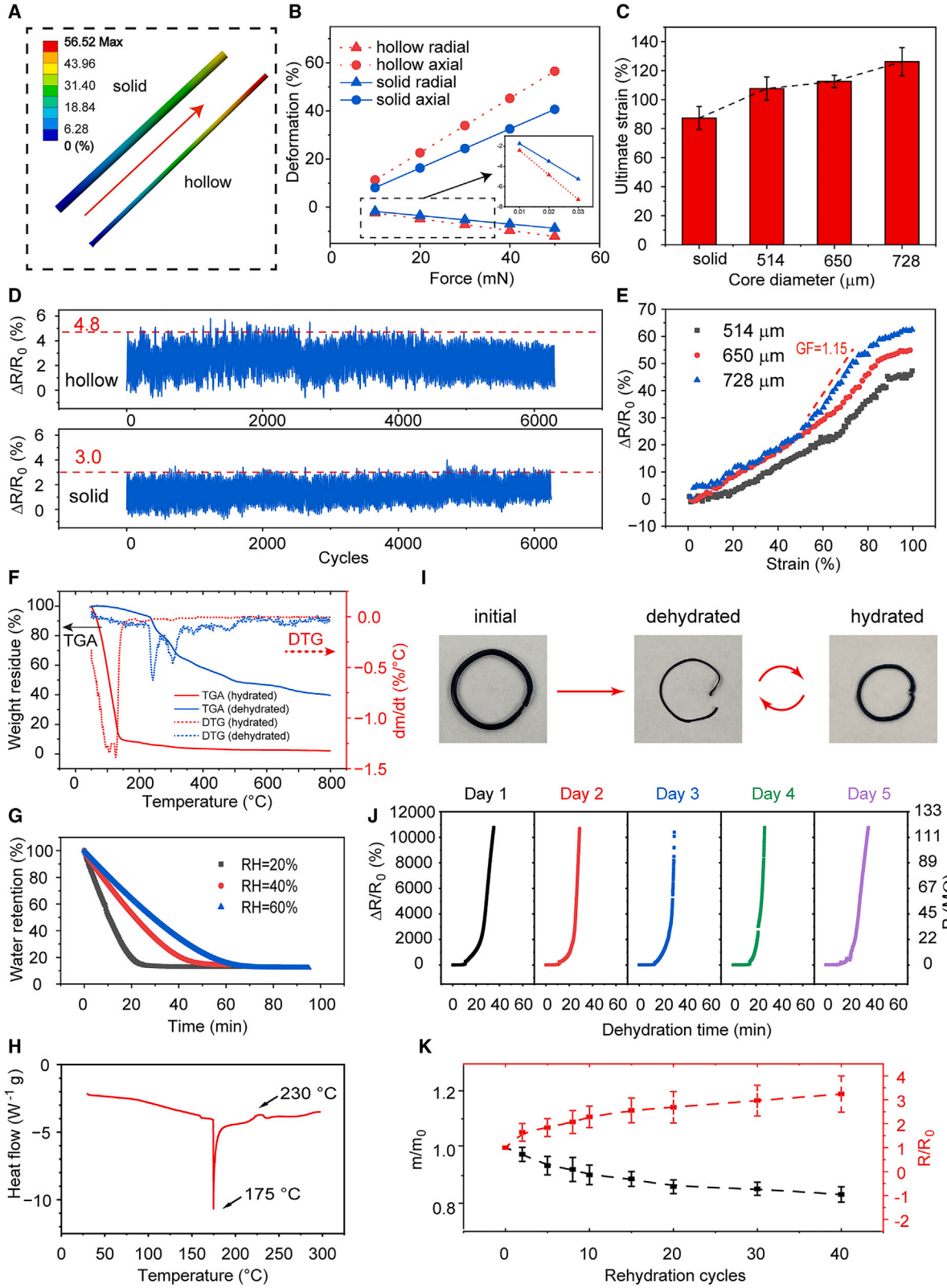
A
56.52 Max
43.96
31.40
18.84
6.28
0 (%)
solid
hollow
B
hollow radial
hollow axial
solid radial
solid axial
Deformation (%)
Force (mN)
C
Ultimate strain (%)
solid
514
650
728
Core diameter (μm)
D
ΔR/R0 (%)
4.8
hollow
3.0
solid
Cycles
E
514 μm
650 μm
728 μm
GF=1.15
ΔR/R0 (%)
Strain (%)
F
Weight residue (%)
TGA
DTG
TGA (hydrated)
TGA (dehydrated)
DTG (hydrated)
DTG (dehydrated)
dm/dt (%/°C)
Temperature (°C)
I
initial
dehydrated
hydrated
G
Water retention (%)
RH=20%
RH=40%
RH=60%
Time (min)
J
Day 1
Day 2
Day 3
Day 4
Day 5
ΔR/R0 (%)
R (MΩ)
Dehydration time (min)
H
Heat flow (W-1 g)
230 °C
175 °C
Temperature (°C)
K
m/m0
R/R0
Rehydration cycles

Figure 3. Characterization of mechanical properties, electrical properties, and reusability of conductive hollow hydrogel fibers
(A and B) FEA demonstrating the deformation of solid and hollow fibers.
(C) Ultimate strain comparison of solid and hollow fibers with different core diameters (data are represented as means ± SD).
(D) Cycling behaviors of solid and hollow fibers under stretching testing.
(E) The strain-dependent resistance changes of hollow fibers with different diameters.
(F) TGA and DTG curves of hydrated and dehydrated conductive hollow hydrogel fibers.
(G) Dynamic vapor sorption curves of conductive hollow hydrogel fibers under varying humidity.
(H) Differential scanning calorimetry thermograms of dehydrated conductive hydrogels.
(I) Photos showing the rehydration cycles of conductive hydrogel.
(J) Real-time resistance changes during the dehydration process of hydrogel over 5 days.
(K) Mass and resistance changes of the conductive hollow hydrogel fibers as a function of rehydration cycle numbers (data are represented as means ± SD).

distribution of Ca-Alg and PEDOT:PSS within the hydrogel network (Figure 2M). These findings underscore the flexibility that co-axial microfluidic printing offers, enabling varied geometry and diameter designs for hollow hydrogel fibers. This versatility enhances its applicability across various uses, especially in high-throughput microfluidics and sensing applications requiring customized fibers.

High-sensitivity conductive hollow hydrogel fibers

As discussed, the hydrogel fibers' electrical, mechanical, cyclical, and reusable properties play a pivotal role, defining their application in flexible and conductive circuits, wearable electronics, soft robotics, and bio-medical devices. Therefore, to investigate the advantages of hollow fibers, we conducted a comparative analysis of solid and hollow fibers. Employing finite element analysis (FEA), we compared the deformation of solid fibers (1 mm diameter) versus hollow fibers (0.8 mm inner diameter) subjected to a gradually increasing tensile load, ranging from 10 to 50 mN, applied to one end while the other end was fixed. The results revealed that the hollow fibers are more stretchable than the solid ones when stretched with 50 mN force applied at one side (Figure 3A). Similarly, under the same load, the axial and radial deformation analysis indicated that the hollow fibers were 40% more highly deformed in both the axial and radial directions (Figure 3B).

Furthermore, the ultimate strains of the solid and hollow fibers with varying core diameters, corresponding to different flow rates, were determined using the ADMET Load Frame (Figures 3C and S12). It can be noted that solid fibers are more brittle than hollow fibers, aligning with the FEA results. The fibers with larger core diameters demonstrated higher ultimate strain and flexibility. These enhanced stretchability, deformability, and ultimate strain rates can be attributed to the hollow structure of the hydrogels, resulting from the low density and the even distribution of the material at the perimeter of the fibers. This enhanced structural stability, along with increased sensitivity to deformation, highlights their potential for detecting subtle motions and lightweight objects.

The electrical performance of solid and hollow fibers was evaluated through a cycling test of resistance changes during stretching. Both solid and hollow fibers were stretched under a strain of 20% at a frequency of 50 Hz using a dynamic motion cycling platform. Notably, the hollow fiber with a 514 μm inner diameter exhibited a considerably higher average resistance change of 4.8% than the solid fiber (3.0%) (Figure 3D). Figure 3E illustrates strain-dependent resistance changes of hollow fibers with diameters of 514, 650, and 728 μm. These results revealed a proportional relationship between the sensitivity and the inner diameter, indicating an increased sensitivity with increasing inner diameter. A gauge factor of 1.15 was calculated between 30% and 50% strain in fibers with a diameter of 728 μm.

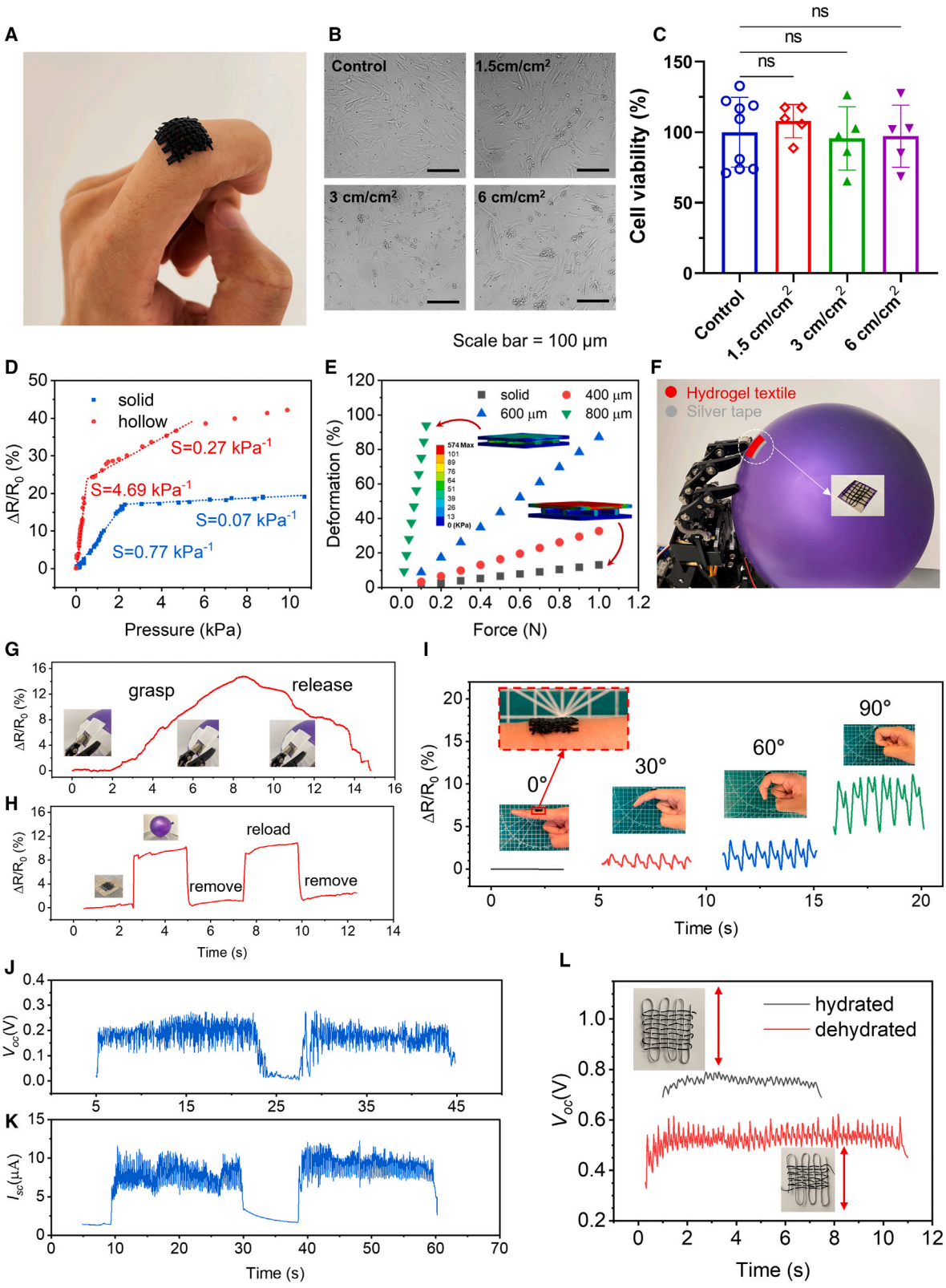
A
B
Control
1.5cm/cm²
3 cm/cm²
6 cm/cm²
Scale bar = 100 μm
C
ns
ns
ns
Cell viability (%)
Control
1.5 cm/cm²
3 cm/cm²
6 cm/cm²
D
solid
hollow
S=0.27 kPa⁻¹
S=4.69 kPa⁻¹
S=0.07 kPa⁻¹
S=0.77 kPa⁻¹
ΔR/R₀ (%)
Pressure (kPa)
E
solid
400 μm
600 μm
800 μm
Deformation (%)
Force (N)
F
Hydrogel textile
Silver tape
G
grasp
release
ΔR/R₀ (%)
H
reload
remove
remove
ΔR/R₀ (%)
Time (s)
I
0°
30°
60°
90°
ΔR/R₀ (%)
Time (s)
J
Voc(V)
K
Isc(μA)
Time (s)
L
hydrated
dehydrated
Voc(V)
Time (s)

Figure 4. Demonstration of bio-compatible conductive hydrogel textiles for motion detection and hybrid textiles for energy harvesting

(A) Optical image of conductive hydrogel textile.

(B) Micrographs of fibroblasts incubated with conductive hollow hydrogel fibers for 3 days (scale bar: 100 μm).

(C) Cytotoxicity of different amounts of conductive hollow hydrogel fibers by MTT assay (data are represented as means ± SD, ns: non-significant).

(D) Pressure-dependent resistance changes of solid and hollow (728 μm) hydrogel textiles.

(E) FEA comparison depicting the deformation of solid and hollow hydrogel textiles with different inner diameters.

(F) Demonstration of conductive hydrogel textile for detection of motion when a robotic hand grasps a balloon. Inset: photograph showing the hydrogel textile attached to the surface of a balloon.

(G) Real-time resistance changes when the robotic hand grasps and releases the balloon. Inset: photos showing a robotic hand grasping and releasing the balloon.

(H) Real-time resistance response of loading and unloading of a balloon.

(I) Resistance changes of the hydrogel textiles in response to different angles of movements of the finger.

(J) The open-circuit voltage (V_{oc}) output of hydrated conductive hollow hydrogel fiber under wrapped contact.

(K) The short-circuit current (I_{sc}) output of dehydrated conductive hollow hydrogel fiber under woven contact.

(L) The V_{oc} output of hydrated and dehydrated hybrid hydrogel woven textiles.

Under the tensile condition, where axial stress is applied, fiber deformation leads to extension, resulting in a disconnection within the PEDOT:PSS network, hindering the hole movement and subsequently increasing the overall resistance. This aligns with the resistance equation ($R = \frac{\rho l}{s}$): as the length increases, the resistance increases accordingly. Moreover, at the same strain, the hollow fiber exhibited a proportional relationship between the inner diameter and the radial deformation, which could account for the higher sensitivity in hollow fibers with larger inner diameters. These results underscore the superior sensing of the printed hollow hydrogel fibers compared to their solid counterparts, paving the way for developing high-sensitivity hydrogel textiles.

The primary factor limiting the conductive hydrogel-based systems' overall performance is dehydration issues, which could potentially lead to a loss of structural integrity, reduced water retention capacity, or altered swelling behavior and biocompatibility. Studying this behavior is essential, and thermogravimetric analysis (TGA) and derivative thermogravimetry (DTG) of both hydrated and dehydrated hydrogels were employed for this purpose. As is shown in Figure 3F, the TGA curve of hydrated hydrogels demonstrated a rapid decline of weight (~90%) in conductive hollow hydrogel fibers under 120°C. Additionally, the DTG of hydrated hydrogels revealed a distinctive peak between 100°C and 125°C, indicating the presence of water content in the conductive hydrogel textile. These findings align with our dynamic vapor sorption shown in Figure 3G, which quantifies the water content at approximately 90% of the hydrogel's total mass. Meanwhile, in the DTG of the dehydrated hydrogels, distinct peaks were observed at 243°C and 304°C, corresponding to the thermal decomposition of the hydrogel's organic polymer compositions. Figure 4H presents the differential scanning calorimetry thermograms of dehydrated conductive hydrogels. The alginate hydrogel exhibited a significant endothermic phase transition at 175°C, reflecting the chain mobility of polymers. Additionally, a broad exothermic peak was observed at 230°C, associated with the decomposition of the polymer through reactions such as decarboxylation and oxidation. These observations are consistent with previous studies.[46]

The rehydration properties of hydrogels position them as potential candidates for reusable sensors, offering sustainable advantages by reducing manufacturing waste. This study investigated the reusability of conductive hollow hydrogel fibers by rehydrating hydrogels (Figure 3I) and examining the changes in performance concerning weight or resistance change over long days (Figure 3J) and rehydration cycles (Figure 3K). In real-time resistance change experiments over a long time (Figure 3J), hydrogel samples were exposed to room temperature conditions to

undergo natural dehydration repeatedly over 5 days. Each cycle involved 24 h of dehydration followed by rehydration of the sample. Our findings indicate significant resistance fluctuations during the dehydration process, occurring within the first hour, but the initial resistance could be decreased again after rehydration. Therefore, we further investigate its performance over long cycles to reveal the reusability performance (Figure 3K).

To simulate the dehydration process, hydrogels were dried under a convection oven at 80°C for 20 min, causing shape shrinkage and water loss within the 3D hydrogel network. Subsequently, the dried fibers were immersed in water at 80°C for 10 min to observe their recovery to their original shapes. Preliminary results indicated that the conductive hollow hydrogel fibers demonstrated a retention of over 97%. Furthermore, to assess the cyclic reforming ability for extended use, we performed 40 dehydration-rehydration cycles of the hydrogels. It was observed that the fibers retained over 80% of their initial weight. In contrast, the resistance increased more than 3-fold, likely due to the loss and redistribution of the PEDOT:PSS dispersed within the hydrogel network. Although the resistance did not fully return to its original state, the rehydration process of the hydrogel demonstrates a degree of reusability that surpasses that of conventional materials. Besides, we further demonstrated the energy harvesting potential of the dehydrated textile and extended its goal for reusability thereafter.

Bio-textile for motion detection and energy harvesting

One promising application of conductive hydrogel textiles is their use in on-skin applications such as bio-electronic and bio-mechanical sensors. To demonstrate the compatibility of the conductive hollow hydrogel textiles for on-skin applications, we developed an on-skin hydrogel textile for motion sensing (Figure 4A). Human dermal fibroblasts were used to examine the cytotoxicity of the hydrogel textile.[47,48] Microscopic examination of cells, as shown in Figure 4B, indicated that the fibroblasts maintained their healthy morphology, characterized by an elongated and dendritic spindle shape, even at concentrations up to 6 cm/cm^2 for 3 days. For quantitative cytotoxicity evaluation, a 3-(4,5-dimethylthiazol-2-yl)-2,5-diphenyltetrazolium bromide (MTT) cell survival assay was employed, with experiments conducted in quintuplicate. The results revealed no apparent cytotoxicity against human dermal fibroblasts (Figure 4C), affirming the bio-compatibility of the conductive hollow hydrogel fibers.

In addition, hydrogel textiles have a wide range of applications, including pressure and motion detection. The woven network, with interconnected fibers and sandwiched between two metal electrodes, establishes a conductive array that allows both in-plane and cross-plane conduction. When subjected to cross-plane forces, the textile deforms, influencing its resistance. To compare the resistance response to applied pressure, we analyzed textiles woven using solid fibers and those woven with hollow fibers. The textiles made with solid fibers exhibited a sensitivity of 0.77 kPa^{-1}. In contrast, our hydrogel textile (728 μm inner diameter) demonstrated a higher sensitivity of 4.69 kPa^{-1} in the small pressure range (<0.5 kPa), an approximately 5-fold increase (Figure 4D). Additionally, FEA was conducted to delve deeper into the differences between solid fibers and hollow fibers with various inner diameters (Figure 4E). Both types of textiles illustrated a linear deformation response to the applied force, but the conductive textile with a hollow structure displayed a significantly sharper response, where a larger inner diameter led to a higher deformation response. This suggests a more sensitive deformation along the radial direction, potentially resulting in higher sensitivity. Furthermore, in addition to the comparison

between fibers with an inner diameter of 728 μm and solid fibers (Figure 4D), the results of the experiments between fibers with diameters of 410 and 650 μm are included in Figure S15. These figures collectively illustrate a proportional relationship between sensitivity and inner diameter. Besides, we demonstrate that the straight hollow structure exhibits higher deformation than the helical structure, possibly due to higher strength conferred by the helical structure (Figures S13 and 14).

To illustrate the potential of the conductive hydrogel textile for human-machine interactions, the textile was utilized as an interfacial sensor, detecting motion when a robotic hand grasps a balloon (Figure 4F). The setup involved the adherence of the hydrogel textile to the balloon's surface via silver tape, while another strip of tape, acting as the counter electrode, was wrapped around the robotic finger. The interaction data revealed a proportional relationship between the object grasping and the resistance: as the robotic hand incrementally held the balloon, the resistance change increased; conversely, as the robotic hand released the balloon, the resistance change decreased (Figure 4G). Notably, the hollow structure showed higher sensitivity in the small pressure range, indicating its potential for detecting lightweight objects. To demonstrate this sensitivity, we recorded the resistance change in response to the presence of an inflated, lightweight balloon (∼6 g) (Figure 4H). The results indicated sharp resistance changes, indicating the presence of the balloon removal, while the resistance nearly returned to the baseline after removal.

Furthermore, to assess the on-skin sensing performance, the conductive hydrogel textile was utilized as a strain sensor for human motion detection (Figure 4I). Specifically, the textile was attached to the joint of a finger, and the bending of the finger induced simultaneous stretching. Consequently, the bending angle could be identified through different resistance changes. Notably, the waveform change was proportional to the bending angle, with a 90° bend leading to resistance changes of 11%, illustrating the textile's precision in capturing subtle human movements.

Additionally, we propose an alternative solution involving the transformation of hybrid textiles for energy harvesting applications during both their hydrated and dehydrated phases using the dynamic Schottky diode methodology, which enables the conversion of mechanical impacts into power output.[49,50] In this technique, conductive fibers function as semiconductors due to PEDOT:PSS forming a dynamic Schottky contact with a metal wire. Depending on the weaving style between the fiber and the metal wire, two types of contacts can be achieved: wrapped contacts and woven contacts. Metal wires and fibers are connected to the anion and cation, respectively, and the movement of the fibers induces friction at the interfaces, generating power. In the wrapped contact configuration, hydrated fiber wraps around the aluminum (Figure 2I), and the contact point depends on the number of rounds, forcing the conductive fiber's movement along the metal wire. In the woven contact scenario, hydrated and dehydrated fibers are interlaced with a single metal wire to form a hybrid textile (Figure 4L). Figure 4J displays the open-circuit voltage under wrapped contact of the hydrated conductive hollow hydrogel fiber, while Figure 4K shows the short-circuit current output under woven contact of the hydrated conductive hollow hydrogel fiber. These results indicate that the short-circuit current output of the hydrated hybrid textile can reach as high as 10 μA with a significant change in the output waveform under woven contact when friction is induced, returning to baseline when movement ceases.

The woven structure creates an m×n matrix of contact points, with friction applied along the metal wires, outputting an open-circuit voltage of ∼0.74 V (average) for

the hydrated hybrid textile. Notably, even when the hybrid hydrogel textile is dehydrated, the output remains around 0.53 V, indicating the durability and resilience of our systems for long-term sustainability (Figure 4L). Compared with the voltage output of wrapped contact (Figure 4J), the woven contact (Figure 4L) has a higher output, primarily due to the greater number of contact points. Therefore, further research on textiles with more on-site contact points can enhance efficiency for energy harvesting and offers a promising avenue for creating self-powered, reusable, environmentally friendly bio-electronic devices that can benefit numerous fields.

DISCUSSION

This study demonstrates a high-sensitivity conductive hydrogel textile with a hollow fiber structure utilizing the co-axial microfluidic printing method. The dimensions and geometry of the enclosed microfluidic channels within the fibers can be controlled according to the Q_{sheath} and Q_{core}. By weaving these conductive hollow hydrogel fibers into a mesh-like 2D structure, we have developed a textile that combines softness, permeability, breathability, and high sensitivity, surpassing the performance of conventional solid structures. The woven hollow hydrogel textile exhibits a sensitivity of 4.69 kPa^{-1}, 6 times that of a solid structure, showcasing its excellent deformation response and potential for motion and deformation detection. Moreover, our research emphasizes the durability and resilience of these hydrogel textiles even after dehydration, indicating their long-term sustainability. The improved sensitivity and intrinsic wearability, coupled with the ability to control fiber geometry and hollow structure dimensions, open up opportunities for the next generation of wearable health monitoring devices, soft actuators for robotics, and electronic skin for prosthetic limbs.

EXPERIMENTAL PROCEDURES

Resource availability

Lead contact

Further information and requests for resources and reagents should be directed to and will be fulfilled by the lead contact, Tian Li (tianli@purdue.edu).

Materials availability

This study did not generate new unique reagents.

Data and code availability

All data needed to evaluate the conclusions in the paper are present in the paper and supplemental information. Additional data related to this paper may be requested from the lead contact.

Materials

PEDOT:PSS conductive ink was made by mixing 95 vol % PEDOT:PSS solution (1.3 wt % dispersion in H_2O, conductive grade) and 5 vol % DMSO (Hybri-Max, sterile filtered, BioReagent, suitable for hybridoma, ≥99.7%). A 4 wt % PEDOT:PSS conductive ink was mixed with Na-Alg at a 1:1 weight ratio to form the conductive gel. $CaCl_2$ (Sigma-Aldrich, St. Louis, MO, USA) was dissolved in deionized water with a concentration of 2 wt %.

Fabrication process of conductive hollow hydrogel fibers and textiles

The spinneret consists of a core flow delivery tube, a two-flow container, and a cone entry. The cone entry and the two-flow container were manufactured by an SLA 3D printer. The liquid resin was pumped into the channel from the upper inclined entrance of the two-flow container. Syringe needles or capillary tubes served as

core flow delivery tubes, where the support liquid was injected into the channel (Figure S2). To ensure that the core flow delivery tube and cone entry are co-axially aligned, the cross-section of the fitting channel of the delivery tube was designed as a square shape. Alignment was achieved by matching the outer diameter of the delivery tube and the inner side of the square cross-section of the fitting channel. The inner diameter and outer diameter of the exit of the cone entry are designed to be 1.5 and 3.5 mm, respectively, and the diameter of the two-flow container is 17 mm. The length of the cylindrical channel is 80 mm, and the total height of the whole device is 125 mm.

The hollow hydrogel microfiber fabrications were carried out in the co-flow spinneret. The inner phase of the 2 wt % $CaCl_2$ stream (acting as a cross-linker) was pumped through a syringe needle with a different rate Q_{core}. In contrast, the outer 2 wt % Na-Alg solution and 0.65 wt % PEDOT:PSS (hydrogel precursor) mixture were injected into the collection cone entry at the rate of Q_{sheath}. A 2 wt % $CaCl_2$ bath was put underneath the tube to collect and store the generated microfiber. The solid hydrogel microfiber was produced by pumping a single flow (2 wt % Na-alginate solutions mixed with 0.65 wt % PEDOT:PSS) into the 2 wt % $CaCl_2$ baths. Hydrogel fibers were woven together for textiles using handcrafted weaving machines.

Morphology characterization of the conductive hollow hydrogel fibers

EDX was conducted on Helios G4 UX dual-beam equipment to observe the characteristic element mapping. To obtain a detailed observation of the hollow and shell structures, the morphology characterization of hydrogel fibers was conducted under cryo-SEM (FEI Nova NanoSEM), where the samples are slushed into liquid nitrogen to retain the structure.

Finite element simulation of the conductive hollow hydrogel fibers and textile

Finite element simulations were performed using commercially available software (ANSYS). A hollow fiber was modeled with a 1,000 μm outer diameter, 800 μm inner diameter, and 25 mm length. The solid fiber has the same outer diameter and length as the hollow fiber. The Young's modulus was set to be 300 kPa, calculated based on the result from the tensile test and a Poisson ratio of 0.4. One end of the circular face was fixed, and tensile stress was applied to the opposite side along the axial direction. The force varied from 0 to 0.05 N. The fiber deformations along the axial and radial directions were recorded. The hydrogel textile was modeled by forming a fiber matrix clamped by the top and bottom metal plates. The bottom metal plate was constrained to be fixed, while the top plate was pushed down with increasing force.

Tensile test of the conductive hollow hydrogel fibers

Tensile tests were conducted using ADMET Load Frame to obtain the stress-strain curves for hollow hydrogel microfibers and solid hydrogel microfibers. To better clamp the samples, sandpaper was attached between the samples and the transducer. Before each test, the initial length and cross-section were measured. Forces were applied along the axial direction of the fibers. The resulting curves would reveal the overall performance of the hydrogel microfiber under displacement, ultimate strains, and stresses for different structures. The error bars and average values of ultimate strains were derived based on the test results of three samples.

Cytotoxicity test of conductive hollow hydrogel fibers

MTT was used in experiments. MTT Cell Growth Assay Kit (CT01), isopropanol (meets USP testing specifications), and HCl (1 N) were purchased from Sigma-Aldrich. Human dermal fibroblasts were maintained in DMEM/F12 medium

(Invitrogen, Grand Island, NY, USA), supplemented by 10% v/v fetal bovine serum, 2 mM L-glutamine, and 100 μg mL^{-1} penicillin/streptomycin. The fibroblasts were cultured in 75 cm^2 T-flasks at 37°C and 5% CO_2 and routinely harvested at 80%–90% confluency using 0.05% trypsin and 0.53 mM EDTA, used for experiments or subculture. The cells were maintained up to the 19th passage during the experiments. The micrographs of cells were acquired by an inverted microscope (IX71, Olympus, Tokyo, Japan) using a 10× objective lens.

Human dermal fibroblasts were seeded in 96-well plates at a density of 500 cells per well and allowed to adhere and develop the dendritic morphology after 2 days of culture at 37°C and 5% CO_2. Cells in each well (0.33 cm^2) were incubated with 0.5, 1, or 2 cm of the polymer for 3 days. After the incubation, the cells were washed with DPBS (Gibco, Grand Island, NY, USA) 3 times, and 100 μL fresh medium was added to each well. The MTT assay started by adding 10 μL MTT to each well, followed by a 4 h incubation for cleavage at 37°C. Then, 100 μL isopropanol with 0.04 N HCl was added to each well and mixed thoroughly with the medium by repeated pipetting. The result was studied with a test wavelength of 570 nm and a reference wavelength of 630 nm using a Microplate Spectrophotometer. The results are presented as means ± SD. Statistical analysis of the cytotoxicity data was performed using GraphPad Prism 9 (La Jolla, CA,USA), employing Student's t test ($p < 0.05$) to determine the statistical significance.

Sensing performance of the conductive hollow hydrogel fibers and textiles

The hydrogel fibers were cut into 60 mm each, and each end of the fiber was pressed by an aluminum plate and taped around a microscope slide. Then, hot glue was utilized to fix the fiber on the slide further. Positive and negative terminals of a digital multimeter were connected to the aluminum plates to measure the resistance and capacitance changes. One end of the setup was taped on the stationary side of the linear stage; another was mounted on the moving stage. The testing length of this microfiber was set to 20 mm. Different strain-dependent resistance change tests were conducted, and real-time resistance change was recorded: (1) the microfiber was stretched by a linear stage with a 5 mm increment each time until it was 100% back to its original length. (2) The linear stage pulled the microfibers to move forward and backward under a 20% stretch. (3) The cycling tests of the microfibers under 20% stretch were tested by reciprocating the stage to stretch the fibers back and forth.

The hydrogel textile was clamped by the top and bottom metal plates, where the bottom plate was fixed and the top plate was adhered with the force gauge (FC10, TORBAL). The force gauge was installed on the Force Gauge Stand with a controllable moving stage. The moving stage of the stand pushed the gauge and the top plate down and pressed on the hydrogel textiles, where the real-time pressure and resistance were recorded. All the resistance changes and voltage outputs were recorded by the multimeter DMM6500 (Keithley).

SUPPLEMENTAL INFORMATION

Supplemental information can be found online at https://doi.org/10.1016/j.xcrp.2024.102047.

ACKNOWLEDGMENTS

The authors acknowledge support from the David and Lucile Packard Foundation. This study was partially supported by a grant from NSF (MCB-2134603) and a Program Grant from the Purdue Institute of Drug Discovery.

AUTHOR CONTRIBUTIONS

Conceptualization, T.L. and P.D.; methodology, P.D., Z.H., and Y.S.; validation, P.D., Z.H., and Y.S.; investigation, P.D., Z.H., Y.S., N.M.M., and W.X.; writing – original draft, P.D.; writing – review & editing, P.D., T.L., Z.H., N.M.M., Y.S., and B.H.; visualization, P.D. and Z.H.; funding acquisition, T.L. and B.H.; resources, T.L. and B.H.; supervision, T.L.

DECLARATION OF INTERESTS

The authors declare no competing interests.

Received: December 12, 2023
Revised: March 30, 2024
Accepted: May 21, 2024
Published: June 13, 2024

REFERENCES

1. Ha, K.H., Zhang, W., Jang, H., Kang, S., Wang, L., Tan, P., Hwang, H., and Lu, N. (2021). Highly Sensitive Capacitive Pressure Sensors over a Wide Pressure Range Enabled by the Hybrid Responses of a Highly Porous Nanocomposite. Adv. Mater. *33*, e2103320. https://doi.org/10.1002/adma.202103320.

2. Lee, S., Franklin, S., Hassani, F.A., Yokota, T., Nayeem, M.O.G., Wang, Y., Leib, R., Cheng, G., Franklin, D.W., and Someya, T. (2020). Nanomesh pressure sensor for monitoring finger manipulation without sensory interference. Science *370*, 966–970. https://doi.org/10.1126/science.abc9735.

3. Meng, K., Xiao, X., Wei, W., Chen, G., Nashalian, A., Shen, S., Xiao, X., and Chen, J. (2022). Wearable Pressure Sensors for Pulse Wave Monitoring. Adv. Mater. *34*, e2109357. https://doi.org/10.1002/adma.202109357.

4. Chen, F., Zhuang, Q., Ding, Y., Zhang, C., Song, X., Chen, Z., Zhang, Y., Mei, Q., Zhao, X., Huang, Q., and Zheng, Z. (2023). Wet-Adaptive Electronic Skin. Adv. Mater. *35*, e2305630. https://doi.org/10.1002/adma.202305630.

5. Zhou, Z., Chen, K., Li, X., Zhang, S., Wu, Y., Zhou, Y., Meng, K., Sun, C., He, Q., Fan, W., et al. (2020). Sign-to-speech translation using machine-learning-assisted stretchable sensor arrays. Nat. Electron. *3*, 571–578. https://doi.org/10.1038/s41928-020-0428-6.

6. Wang, Y., Yin, L., Bai, Y., Liu, S., Wang, L., Zhou, Y., Hou, C., Yang, Z., Wu, H., Ma, J., et al. (2020). Electrically compensated, tattoo-like electrodes for epidermal electrophysiology at scale. Sci. Adv. *6*, eabd0996. https://doi.org/10.1126/sciadv.abd0996.

7. Jang, H., Sel, K., Kim, E., Kim, S., Yang, X., Kang, S., Ha, K.H., Wang, R., Rao, Y., Jafari, R., and Lu, N. (2022). Graphene e-tattoos for unobstructive ambulatory electrodermal activity sensing on the palm enabled by heterogeneous serpentine ribbons. Nat. Commun. *13*, 6604–6613. https://doi.org/10.1038/s41467-022-34406-2.

8. Xu, J., Tat, T., Yin, J., Ngo, D., Zhao, X., Wan, X., Che, Z., Chen, K., Harris, L., and Chen, J. (2023). A textile magnetoelastic patch for self-powered personalized muscle physiotherapy. Matter *6*, 2235–2247. https://doi.org/10.1016/j.matt.2023.06.008.

9. Li, S., Zhang, Y., Wang, Y., Xia, K., Yin, Z., Wang, H., Zhang, M., Liang, X., Lu, H., Zhu, M., et al. (2020). Physical sensors for skin-inspired electronics. InfoMat *2*, 184–211. https://doi.org/10.1002/inf2.12060.

10. Ma, Y., Cheng, Y., Wang, J., Fu, S., Zhou, M., Yang, Y., Li, B., Zhang, X., and Nan, C.W. (2022). Flexible and highly-sensitive pressure sensor based on controllably oxidized MXene. InfoMat *4*, 1–12. https://doi.org/10.1002/inf2.12328.

11. Lu, Y., Yue, Y., Ding, Q., Mei, C., Xu, X., Jiang, S., He, S., Wu, Q., Xiao, H., and Han, J. (2023). Environment-tolerant ionic hydrogel–elastomer hybrids with robust interfaces, high transparence, and biocompatibility for a mechanical–thermal multimode sensor. InfoMat *5*, 1–18. https://doi.org/10.1002/inf2.12409.

12. Xu, H., Gao, L., Wang, Y., Cao, K., Hu, X., Wang, L., Mu, M., Liu, M., Zhang, H., Wang, W., and Lu, Y. (2020). Flexible Waterproof Piezoresistive Pressure Sensors with Wide Linear Working Range Based on Conductive Fabrics. Nano-Micro Lett. *12*, 159. https://doi.org/10.1007/s40820-020-00498-y.

13. Ma, H., Qin, H., Xiao, X., Liu, N., Wang, S., Li, J., Shen, S., Dai, S., Sun, M., Li, P., et al. (2023). Robust hydrogel sensors for unsupervised learning enabled sign-to-verbal translation. InfoMat *5*, 1–11. https://doi.org/10.1002/inf2.12419.

14. Wen, J., Wu, Y., Gao, Y., Su, Q., Liu, Y., Wu, H., Zhang, H., Liu, Z., Yao, H., Huang, X., et al. (2023). Nanofiber Composite Reinforced Organohydrogels for Multifunctional and Wearable Electronics. Nano-Micro Lett. *15*, 174. https://doi.org/10.1007/s40820-023-01148-9.

15. Liu, X., Zhu, W., Deng, P., and Li, T. (2023). Redesigning Natural Materials for Energy, Water, Environment, and Devices. ACS Nano *17*, 18657–18668. https://doi.org/10.1021/acsnano.3c04065.

16. Hao, H., Wu, S., Lin, J., Zheng, Z., Zhou, Y., Zhang, Y., Guo, Q., Tian, F., Zhao, M., Chen, Y., et al. (2023). Immunization against Zika by entrapping live virus in a subcutaneous self-adjuvanting hydrogel. Nat. Biomed. Eng. *7*, 928–942. https://doi.org/10.1038/s41551-023-01014-4.

17. He, Y., Li, Q., Chen, P., Duan, Q., Zhan, J., Cai, X., Wang, L., Hou, H., and Qiu, X. (2022). A smart adhesive Janus hydrogel for non-invasive cardiac repair and tissue adhesion prevention. Nat. Commun. *13*, 7666. https://doi.org/10.1038/s41467-022-35437-5.

18. Hu, L., Chee, P.L., Sugiarto, S., Yu, Y., Shi, C., Yan, R., Yao, Z., Shi, X., Zhi, J., Kai, D., et al. (2023). Hydrogel-Based Flexible Electronics. Adv. Mater. *35*, e2205326–e2205332. https://doi.org/10.1002/adma.202205326.

19. Tian, H., Wang, C., Chen, Y., Zheng, L., Jing, H., Xu, L., Wang, X., Liu, Y., and Hao, J. (2023). Optically modulated ionic conductivity in a hydrogel for emulating synaptic functions. Sci. Adv. *9*. eadd6950–11. https://doi.org/10.1126/sciadv.add6950.

20. Won, D., Kim, J., Choi, J., Kim, H., Han, S., Ha, I., Bang, J., Kim, K.K., Lee, Y., Kim, T.S., et al. (2022). Digital selective transformation and patterning of highly conductive hydrogel bioelectronics by laser-induced phase separation. Sci. Adv. *8*, eabo3209. https://doi.org/10.1126/sciadv.abo3209.

21. Guo, R., Fang, Y., Wang, Z., Libanori, A., Xiao, X., Wan, D., Cui, X., Sang, S., Zhang, W., Zhang, H., and Chen, J. (2022). Deep Learning Assisted Body Area Triboelectric Hydrogel Sensor Network for Infant Care. Adv. Funct. Mater. *32*, 1–7. https://doi.org/10.1002/adfm.202204803.

22. Qu, S. (2022). 3D printing of hydrogel electronics. Nat. Electron. *5*, 838–839. https://doi.org/10.1038/s41928-022-00900-0.

23. Ge, G., Lu, Y., Qu, X., Zhao, W., Ren, Y., Wang, W., Wang, Q., Huang, W., and Dong, X. (2020). Muscle-Inspired Self-Healing Hydrogels for Strain and Temperature Sensor. ACS Nano *14*, 218–228. https://doi.org/10.1021/acsnano.9b07874.

24. Na, H., Kang, Y.W., Park, C.S., Jung, S., Kim, H.Y., and Sun, J.Y. (2022). Hydrogel-based strong and fast actuators by electroosmotic turgor pressure. Science *376*, 301–307. https://doi.org/10.1126/science.abm7862.

25. Zhao, Y., Lo, C.Y., Ruan, L., Pi, C.H., Kim, C., Alsaid, Y., Frenkel, I., Rico, R., Tsao, T.C., and He, X. (2021). Somatosensory actuator based on stretchable conductive photothermally responsive hydrogel. Sci. Robot. *6*. eabd5483–12. https://doi.org/10.1126/SCIROBOTICS.ABD5483.

26. Wen, N., Fan, Z., Yang, S., Zhao, Y., Cong, T., Xu, S., Zhang, H., Wang, J., Huang, H., Li, C., and Pan, L. (2020). Highly conductive, ultra-flexible and continuously processable PEDOT:PSS fibers with high thermoelectric properties for wearable energy harvesting. Nano Energy *78*, 105361. https://doi.org/10.1016/j.nanoen.2020.105361.

27. Cheng, T., Zhang, Y.Z., Wang, S., Chen, Y.L., Gao, S.Y., Wang, F., Lai, W.Y., and Huang, W. (2021). Conductive Hydrogel-Based Electrodes and Electrolytes for Stretchable and Self-Healable Supercapacitors. Adv. Funct. Mater. *31*, 1–27. https://doi.org/10.1002/adfm.202101303.

28. Li, G., Li, C., Li, G., Yu, D., Song, Z., Wang, H., Liu, X., Liu, H., and Liu, W. (2022). Development of Conductive Hydrogels for Fabricating Flexible Strain Sensors. Small *18*, e2101518. https://doi.org/10.1002/smll.202101518.

29. Gao, Y., Gu, S., Jia, F., and Gao, G. (2020). A skin-matchable, recyclable and biofriendly strain sensor based on a hydrolyzed keratin-containing hydrogel. J. Mater. Chem. A *8*, 24175–24183. https://doi.org/10.1039/d0ta07883b.

30. Jung, H., Kim, M.K., Lee, J.Y., Choi, S.W., and Kim, J. (2020). Adhesive Hydrogel Patch with Enhanced Strength and Adhesiveness to Skin for Transdermal Drug Delivery. Adv. Funct. Mater. *30*, 1–10. https://doi.org/10.1002/adfm.202004407.

31. Li, H., Qu, R., Ma, Z., Zhou, N., Huang, Q., and Zheng, Z. (2023). Permeable and Patternable Super-Stretchable Liquid Metal Fiber for Constructing High-Integration-Density Multifunctional Electronic Fibers. Adv. Funct. Mater. *2308120*, 1–11. https://doi.org/10.1002/adfm.202308120.

32. Deng, P., Li, X., Wang, Y., He, Z., Zhu, W., Zhang, Y., Schalm, G.M., and Li, T. (2023). Highly Stretchable Ionic and Electronic Conductive Fabric. Adv. Fiber Mater. *5*, 198–208. https://doi.org/10.1007/s42765-022-00208-w.

33. Huang, Q., and Zheng, Z. (2022). Pathway to Developing Permeable Electronics. ACS Nano *16*, 15537–15544. https://doi.org/10.1021/acsnano.2c08091.

34. Ding, T., Chan, K.H., Zhou, Y., Wang, X.Q., Cheng, Y., Li, T., and Ho, G.W. (2020). Scalable thermoelectric fibers for multifunctional textile-electronics. Nat. Commun. *11*, 6006–6008. https://doi.org/10.1038/s41467-020-19867-7.

35. Shi, Y., Wu, B., Sun, S., and Wu, P. (2023). Aqueous spinning of robust, self-healable, and crack-resistant hydrogel microfibers enabled by hydrogen bond nanoconfinement. Nat. Commun. *14*, 1370. https://doi.org/10.1038/s41467-023-37036-4.

36. Ding, H., Wu, Z., Wang, H., Zhou, Z., Wei, Y., Tao, K., Xie, X., and Wu, J. (2022). An ultrastretchable, high-performance, and crosstalk-free proximity and pressure bimodal sensor based on ionic hydrogel fibers for human-machine interfaces. Mater. Horiz. *9*, 1935–1946. https://doi.org/10.1039/d2mh00281g.

37. Li, M., Chen, X., Li, X., Dong, J., Zhao, X., and Zhang, Q. (2021). Wearable and Robust Polyimide Hydrogel Fiber Textiles for Strain Sensors. ACS Appl. Mater. Interfaces *13*, 43323–43332. https://doi.org/10.1021/acsami.1c10055.

38. Shuai, L., Guo, Z.H., Zhang, P., Wan, J., Pu, X., and Wang, Z.L. (2020). Stretchable, self-healing, conductive hydrogel fibers for strain sensing and triboelectric energy-harvesting smart textiles. Nano Energy *78*, 105389. https://doi.org/10.1016/j.nanoen.2020.105389.

39. Costantini, M., Colosi, C., Święszkowski, W., and Barbetta, A. (2018). Co-axial wet-spinning in 3D bioprinting: State of the art and future perspective of microfluidic integration. Biofabrication *11*, 012001. https://doi.org/10.1088/1758-5090/aae605.

40. Xu, P., Xie, R., Liu, Y., Luo, G., Ding, M., and Liang, Q. (2017). Bioinspired Microfibers with Embedded Perfusable Helical Channels. Adv. Mater. *29*, 1–7. https://doi.org/10.1002/adma.201701664.

41. Yu, Y., Fu, F., Shang, L., Cheng, Y., Gu, Z., and Zhao, Y. (2017). Bioinspired Helical Microfibers from Microfluidics. Adv. Mater. *29*, 1605765. https://doi.org/10.1002/adma.201605765.

42. Hu, M., Deng, R., Schumacher, K.M., Kurisawa, M., Ye, H., Purnamawati, K., and Ying, J.Y. (2010). Hydrodynamic spinning of hydrogel fibers. Biomaterials *31*, 863–869. https://doi.org/10.1016/j.biomaterials.2009.10.002.

43. Zarrin, F., and Dovichi, N.J. (1985). Sub-Picoliter Detection with the Sheath Flow Cuvette. Anal. Chem. *57*, 2690–2692. https://doi.org/10.1021/ac00290a057.

44. Kong, D.C., Yang, M.H., Zhang, X.S., Du, Z.C., Fu, Q., Gao, X.Q., and Gong, J.W. (2021). Control of Polymer Properties by Entanglement: A Review. Macromol. Mater. Eng. *306*, 1–20. https://doi.org/10.1002/mame.202100536.

45. Atencia, J., and Beebe, D. (2005). Controlled microfluidic interfaces. Nature *437*, 648–655. https://doi.org/10.1038/nature04163.

46. Falkeborg, M., Paitaid, P., Shu, A.N., Pérez, B., and Guo, Z. (2015). Dodecenyl succinylated alginate as a novel material for encapsulation and hyperactivation of lipases. Carbohydr. Polym. *133*, 194–202. https://doi.org/10.1016/j.carbpol.2015.06.103.

47. Shen, Y., Shah, S.R., Zhao, K., and Han, B. (2023). Experimental and computational analysis of the injection-induced mechanical changes in the skin microenvironment during subcutaneous injection of biologics. Extreme Mech. Lett. *61*, 102025. https://doi.org/10.1016/j.eml.2023.102025.

48. Park, S., Seawright, A., Park, S., Craig Dutton, J., Grinnell, F., and Han, B. (2015). Preservation of tissue microstructure and functionality during freezing by modulation of cytoskeletal structure. J. Mech. Behav. Biomed. Mater. *45*, 32–44. https://doi.org/10.1016/j.jmbbm.2015.01.014.

49. Deng, P., Wang, Y., Yang, R., He, Z., Tan, Y., Chen, Z., Liu, J., and Li, T. (2023). Self-Powered Smart Textile Based on Dynamic Schottky Diode for Human-Machine Interactions. Adv. Sci. *10*, e2207298–e2207299. https://doi.org/10.1002/advs.202207298.

50. Liu, J., Goswami, A., Jiang, K., Khan, F., Kim, S., McGee, R., Li, Z., Hu, Z., Lee, J., and Thundat, T. (2018). Direct-current triboelectricity generation by a sliding Schottky nanocontact on MoS2 multilayers. Nat. Nanotechnol. *13*, 112–116. https://doi.org/10.1038/s41565-017-0019-5.